Advanced usage of $Ti_3C_2T_x$ MXenes for photothermal therapy on different 3D breast cancer models

Giordano Perini [a,b,1], Andreas Rosenkranz [c,1], Ginevra Friggeri [a], Dario Zambrano [c], Enrico Rosa [a], Alberto Augello [a], Valentina Palmieri [a,b,d,*], Marco De Spirito [a,b], Massimiliano Papi [a,b,*]

[a] Dipartimento di Neuroscienze, Università Cattolica del Sacro Cuore, Largo Francesco Vito 1, 00168 Rome, Italy
[b] Fondazione Policlinico Universitario A. Gemelli IRCSS, 00168 Rome, Italy
[c] Department of Chemical Engineering, Biotechnology and Materials, FCFM, University of Chile, Santiago 8370415, Chile
[d] Istituto dei Sistemi Complessi, CNR, Via dei Taurini 19, 00185 Rome, Italy

ARTICLE INFO

ABSTRACT

Globally, breast cancer is the most diagnosed invasive cancer among women. Current therapies (*e.g.*, chemotherapy) show numerous limitations due to the lack of selectivity and involved side effects, which urgently asks for novel approaches with enhanced tumor-killing efficacy. We previously demonstrated that MXenes, new bioactive nanomaterials with promising photophysical properties, are capable to increase the efficiency of the targeted breast cancer photothermal therapy (PTT). In this work, we investigated the effect of few- and multi-layer $Ti_3C_2T_x$ MXenes mediated-PTT on two different 3D reliable breast cancer models such as conventional and bio-printed spheroids. We performed PTT on both cancer models using a non-toxic MXene concentration of 50 μg/mL. After PTT, a significant reduction in the cell viability along with a notable increase in reactive oxygen species (ROS) was observed. Moreover, we studied the effect of PTT on the migration of macrophages and endothelial cells toward cancer regions in both 3D models. Our results indicate that PTT mediated by both few- and multi-layer MXenes significantly modulates the tumor progression through cells' death by increasing the temperature, which holds particularly true for the bio-printed model.

1. Introduction

Globally, breast cancer is the most diagnosed invasive cancer and the first reason of cancer-related death among women. More than 1.5 million women are diagnosed with breast cancer each year all over the world thus making it the most frequent cancer across all age groups [1, 2]. Breast cancer is categorized into three major subtypes based on the presence or absence of molecular markers for estrogen or progesterone receptors and human epidermal growth factor 2 (ERBB2; formerly HER2): hormone receptor-positive/ERBB2 negative (70 % of patients), ERBB2 positive (15–20 %), and triple-negative (tumors lacking all three standard molecular markers; 15 %) [3]. Triple-negative breast cancer is more likely to recur, while surgery or chemotherapy are the only feasible therapies due to the lack of receptors on these cell types. In clinical practice, chemotherapy is one of the main treatments available.

However, it shows numerous limitations due to the lack of selectivity and involved side effects leading to patients' discomfort.

A promising alternative strategy for cancer treatment is photothermal therapy (PTT), which is a non-invasive technique. PTT is based on the absorption and conversion of near-infrared radiation (NIR) into heat by several molecules, namely photosensitizers, such as graphene [4–6] and quantum dots [7,8]. NIR can deeply penetrate tissues, and, for this reason, PTT has recently emerged as an important and efficient strategy for cancer treatment. Moreover, the toxicity of the photosensitizers in physiological tissues is low, resulting in reduced side effects and improved life [9–11]. In this context, we explored the use of $Ti_3C_2T_x$ MXenes, newly emerging bioactive nanomaterials with promising photophysical properties, to increase the efficiency of targeted breast cancer PTT. MXenes are newly evolving 2D nanomaterials that have recently demonstrated their feasibility as theranostic nanoplatforms and, more

---

* Corresponding authors at: Dipartimento di Neuroscienze, Università Cattolica del Sacro Cuore, Largo Francesco Vito 1, 00168 Rome, Italy.
  E-mail addresses: valentina.palmieri@cnr.it (V. Palmieri), massimiliano.papi@unicatt.it (M. Papi).
[1] These authors contributed equally to this work.

importantly, as photosensitizing agents to exert tumor ablation [12]. In this regard, MXenes are highly suitable for PTT due to their biocompatibility and low cytotoxicity. Furthermore, they depicted a higher photothermal conversion than that of other materials, which are commonly used for PTT, such as graphene oxide or gold nanoparticles [13,14].

In this work, MXene-mediated PTT has been tested on two 3D models (with or without extracellular matrix, ECM) to resemble the *in-vivo* structural complexity of cancer [15–17]. 3D cell cultures constitute a recent approach for therapeutic testing, being the link between traditional 2D cell culture and *in-vivo* models [18,19]. The use of spheroids, a 3D structure composed of cancer cells, has proven to be an efficient system for developing *in-vitro* screening with high physiological relevance for the preclinical development of drugs, which holds especially true for the oncological and toxicological fields [20,21]. The power of this approach relies on its ability to mimic many aspects of *in-vivo* tumor conditions while being fast, inexpensive, and versatile enough to allow relatively high-throughput screening. However, the application of this system is limited due to the poor self-renewal and differentiation capacity of the spheroids. Therefore, recent advances in 3D cultures and bio-printing have focused on the development of spheroid models, in which cells are arranged in a more ordered architecture on specific matrices to mimic tumor-ECM interaction. This alternative provides a higher capacity for self-renewal and prolonged proliferation of cancer cells, along with an augmented interaction with ECM and tumor microenvironment, which resembles the complex *in-vivo* system more appropriately, *i.e.* necrotic core, invasive edges and the tumor microenvironment [22–27].

Therefore, we first investigated the effect of PTT on standard 4T1 spheroids treated with few- (FX) and multi-layer (MX) $Ti_3C_2T_x$ to test the potential effect of the nanomaterial's thickness [28]. Subsequently, we bio-printed a 3D cancer model, in which 4T1 breast cancer cells were embedded in a matrix resembling ECM [23,29–31]. We observed a significant reduction in the cell viability after PTT for both MXenes. ROS production also resulted significantly higher than that of the non-irradiated spheroids. We also explored the migration behavior of the immune and endothelial cells towards cancer aggregates. Our results set the basis for future clinical applications of non-invasive MXenes-based PTT, shortening the path to clinical translation.

2. Materials and methods

2.1. Synthesis and characterization of MXenes

For the synthesis of few- (FX) and multi-layer (MX) $Ti_3C_2T_x$ nanosheets, 5 g of Ti_3AlC_2 precursor (Forsman Scientific Co. Ltd., Beijing, China) were placed in 50 mL of an aqueous HF solution (hydrofluoric acid concentration about 40 %). The solution was magnetically stirred at a constant speed of 60 rpm for one day under environmental conditions and at a slightly elevated temperature of about 35 °C. To obtain MX, the solution was centrifuged for 5 min at 3500 rpm. Afterwards, a neutral pH was adjusted by washing the obtained suspension with deionized water before the respective filtering and drying processes. Filtering was realized by vacuum-assisted filtration using a water circulating vacuum pump with poly-ether-sulfone filter membranes. With respect to the subsequent drying, the solution was stored in a fridge for 8 h at a temperature of − 10 °C before performing freeze-dying step maintaining a temperature of − 60 °C and a pressure below 30 Pa for one day. To generate FX, centrifuged MX were exfoliated in distilled water by ultrasonication for 8 min. Afterwards, the solution was centrifuged at 1550 rpm for 5 min. The supernatant was collected and freeze-dried using the same procedure [32].

2.2. Spectroscopic and microscopic analysis of FX and MX

Transmission electron microscopy (TEM, Tecnai F20, FEI) using an

acceleration voltage of 200 kV was utilized to check the structure of the as-produced FX and MX. Using an EDAX detector, the chemical composition of the nano-sheets was studied. Powder X-Ray diffraction (XRD, PANalytical Empyrean) was conducted in Bragg-Brentano configuration with CuKα irradiation using 40 kV and 40 mA (step size: 0.026° and the dwell time: 1396.89 s). Raman spectra (Alpha 300 RA, Witec) were acquired by averaging 256 accumulations with an integration time of 4 s and utilizing an excitation wavelength of 633 nm, a grating of 300 g/mm, and 10 % of the maximum laser intensity. Non-monochromatic AlKα radiation was used to perform X-Ray photoelectron spectroscopy (XPS, Physical Electronics 1257) with constant source settings at 15 kV and 400 W as well as a pass energy of 44.75 eV. The overall surface composition was assessed by coarser scans with binding energies (BE) ranging from 1000 to 0 eV using a step size of 1 eV. Finer scans of the C_{1s} and Ti_{2p} peaks were recorded with a step size of 0.1 eV. The C_{1s} peak was fitted with Lorentz-Gaussian functions. Regarding the background subtraction, a linear correction was used for the Ti_{2p} peak, while the remaining photoelectron peaks were baseline corrected by the Shirley method [32].

2.3. Photothermal effect of FX and MX

To assess the photothermal effect of FX and MX, samples at 25, 50, and 100 μg/mL in double-distilled water (Milli-Q) were irradiated using an 808 nm laser (Laser Ever) for 3 min. Three different power densities were adjusted for FX and MX to induce the same thermal effect (2.3, 1.3 and 0.6 W/cm^2 for MX and 1.3, 0.8, and 0.4 W/cm^2 for FX at concentrations of 25, 50, and 100 μg/mL, respectively). A thermal imaging camera (Optris) was used to record the temperature of the solution.

2.4. Cell culture

The 4T1 mouse mammary tumor cell line was purchased from the American Type Culture Collection (ATTC, Manassas, VA, USA). Cells were maintained in Dulbecco's modified Eagle's medium (DMEM, Sigma-Aldrich, St. Louis, MO, USA) supplemented with 10 % fetal bovine serum (FBS, EuroClone), 2 % penicillin-streptomycin (Sigma-Aldrich, St. Louis, MO, USA) and 2 % L-glutamine (Sigma-Aldrich, St. Louis, MO, USA). Cells were cultivated in T75 flasks and kept at 37 °C and 5 % CO_2. The RAW 264.7 murine macrophage cell line (ATCC® CRL1469™) and the hybrid clone EA.hy926 human umbilical vein cell line (ATCC® CRL2922™) were purchased from the ATCC and maintained in DMEM (Sigma-Aldrich, St. Louis, MO, USA) supplemented with 10 % FBS (EuroClone), 2 % penicillin-streptomycin (Sigma-Aldrich, St. Louis, MO, USA), 2 % L-glutamine (Sigma-Aldrich, St. Louis, MO, USA), 2 mM sodium pyruvate (Sigma-Aldrich), and 1500 mg/L sodium bicarbonate (Sigma-Aldrich). Cells were cultivated in T75 flasks and kept at 37 °C and 5 % CO_2.

2.5. Biocompatibility of FX and MX on 2D models

For the experiments regarding biocompatibility, MX was centrifuged at 500 g for 30 s, while FX was centrifuged at 1000 *g* for 30 s, to remove big and not-dissolved nano-sheets. The concentration was determined by preparing a calibration curve prior to centrifugation. To evaluate the biocompatibility of MX and FX, 4T1 cells were seeded on 96-well plates (Corning) at a seeding density of 10^5 cells/mL. Cells were treated with MX and FX at different concentrations: 25, 50, and 100 μg/mL. 24 h after administration, biocompatibility and cytotoxicity were evaluated in terms of cell viability and production of ROS. To measure the cell viability, CellTiter-Glo (Promega) was added to each well with a volume equal to culture medium, and shaken for 2 min in an orbital shaker to induce cell lysis. Plates were incubated at room temperature for 10 min before recording luminescence using a Cytation 3 Cell Imaging Multi-Mode Reader (Biotek). The viability was expressed as the percentage of the untreated (control) cells.

For the detection of ROS, the fluorinated derivative of 2′,7′-dichlorofluorescein (H$_2$DCFDA) was employed. This probe is nonfluorescent until the acetate groups are removed by intracellular esterases and oxidation occurs within cells. Thus, oxidation can be detected by monitoring the increase in the fluorescence intensity. After the treatment with MXenes, the medium containing non-internalized MX and FX was replaced with PBS containing 10 μM H$_2$DCFDA. Cells were incubated for 30 min at 37 °C in 5 % CO$_2$. PBS containing H$_2$DCFDA was then removed, and cells were resuspended in complete medium. The fluorescence intensity of H$_2$DCFDA was recorded by using a Cytation 3 Cell Imaging Multi-Mode Reader using an excitation wavelength of 495 nm and recording the emission at 528 nm.

2.6. 3D Model preparation and viability tests

2.6.1. Spheroid preparation

4T1 mouse mammary tumor cells were seeded on 96-well, round bottom, ultra-low attachment plate (Corning, Corning, NY, USA) at a density of 0.5×10^5 cells/mL. The multi-well was centrifuged at 300 *g* for 3 min to ensure the confluence of cells to the center of the wells [33]. The so-formed spheroids were incubated at 37 °C in 5 % CO$_2$ for 3 days before further treatment. Spheroids were then treated with FX and MX at a concentration of 50 μg/mL. Experiments were carried out within the next four days from the administration of FX and MX. Transmittance images of spheroids were collected using Cytation 3 Cell Imaging Multi-Mode Reader.

2.6.2. Bioprinting of 4T1 3D model

To perform experiments on 3D models of 4T1 mouse mammary tumor cells in presence of extracellular components, cancer spheroids were produced *via* bio-printing [25] using a droplet printing (BIOX Cellink). Precisely, 3×10^6 cells/mL were mixed with 5 % alginate (Sigma-Aldrich) in a syringe with a 1:1 ratio. Cells mixed with the hydrogel were loaded on a bioprinting cartridge. Spheroid droplets were released on a 96-well round-bottom previously filled with 100 μL of 2 % CaCl$_2$ to induce crosslinking. Droplets were incubated for 5 min at room temperature, then CaCl$_2$ was replaced with fresh complete culture medium. Spheroid droplets were then incubated at 37 °C and 5 % CO$_2$ for further treatment.

2.6.3. Viability and production of ROS on 4T1 spheroids

Cell viability was measured after 48 and 96 h on spheroids and bio-printed spheroids. The viability tests were performed using the CellTiter-Glo® Luminescent Cell Viability Assay (Promega, Madison, WI, USA), which was added to each well and shaken for 5 min in an orbital shaker to induce cell lysis. Plates were incubated at room temperature for 20 min under dark conditions before luminescence was recorded. For the detection of ROS, the CellROX® green reagent was employed following manufacturer's instructions. Briefly, the reagent was added at a final concentration of 5 μM and incubated for 30 min at 37 °C. After 30 min, the signal of the fluorescence intensity was analyzed using an excitation wavelength of 485 nm and recording the emission at 520 nm utilizing a Cytation3 Cell Imaging Multi-Mode Reader. The obtained results were normalized by the number of viable cells for each treatment.

2.6.4. Migration of RAW 264.7 and EA.hy926 by PTT

To test the effect of PTT on the migration of macrophages and endothelial cells, NIR therapy was carried out on both 4T1 spheroids and bio-printed spheroids at 24 and 72 h after the administration of 50 μg/mL FX and MX. After the treatment, the supernatant of the spheroids was collected and transferred to the lower chamber of a transwell system at a final volume of 600 μL. RAW 264.7 murine macrophages or EA.hy926 human endothelial cells were seeded on the upper chamber of the transwell system (5 μm pore size) at a seeding density of 10^5 cells/mL. After 24 h of incubation, calcein was added to the lower and the upper chamber at a final concentration of 10 μM, and the multiwell was

incubated for 30 min at 37 °C at 5 % CO$_2$. Following the incubation, the fluorescence intensity of calcein was recorded on both sides of the transwell by exciting at 480 nm and recording emission at 535 nm.

3. Results and discussion

3.1. Characterization of FX and MX MXenes

The initial structural characterization of the as-synthesized few- and multi-layer Ti$_3$C$_2$T$_x$ nanosheets MXenes was done by high-resolution TEM. The TEM results depicted in Fig. 1 (**a** and **b**) demonstrate the layered structure of FX and MX. Based upon statistical analysis, FX nano-sheets consist of an average of about 15 layers, while MX nano-sheets are much thicker in z-direction having about 90–100 layers. Irrespective of the nano-sheets considered, the lateral dimensions were similar (∼ 2 μm). TEM-EDX detected only minor remaining traces of Al originating from the parental MAX-phase Ti$_3$AlC$_2$ (about 0.5 wt%), thus confirming an efficient etching process, which produces MXenes with a high purity.

Subsequently, detailed XPS scans of the C$_{1 s}$, Ti$_{2p}$, and O$_{1 s}$ region for FX and MX nano-sheets were recorded as presented in Fig. 1 (**c–h**). According to Fig. 1 (**c** and **d**), four fit functions are needed to adequately fit the C$_{1 s}$ region for both nano-sheets. Irrespective of the nano-sheets considered, similar superficial bonding states with contributions originating from C-C bonds and adventitious carbon (284.8 eV), C-Ti-T$_x$ (281.7 eV), hydrocarbons (286.5, eV), and C-F bonds (288.5 eV) are detected. Related to the Ti$_{2p}$ peak Fig. 1 (**e** and **f**), three doublets with variable relative intensities need to be considered for both nano-sheets. Concerning FX, the contribution at 455.0 eV (titanium carbides (MXenes)) has a relative contribution of 22 %. Peaks located at 456.8 and 459.2 eV reflect higher oxidation states of Ti. For MX, the peak assignable to titanium carbides (MXenes) located at 454.9 eV makes up about 62 %. The two remaining contributions with lower relative intensities are attributable to C-Ti-(O or OH) and C-Ti-O [34–37]. With respect to the O$_{1 s}$ region (Fig. 1 (**g** and **h**), two main contributions stemming from metal oxides and hydroxides can be observed. In case of FX, about 55 % of the superficial bonding states are metal oxides (TiO$_2$ or more generally Ti(IV)), while the remaining 45 % can be assigned to hydroxides. In contrast, MX demonstrated an increased relative number of hydroxides (90 %) and only 10 % metal oxides. For both nano-sheets, the hydroxide contribution matches with the existing -OH surface terminations (C-Ti-(OH)$_x$).

Finally, Raman spectra of FX and MX present similar Raman vibrations as displayed in Fig. 1 **i.** In case of FX, peaks are detectable at 129, 159, 208, 381, 592, and 705 cm^{-1}, while MX shows peaks at 125, 212, 285, 376, 600 and 701 cm^{-1}. The intensity of the detected Raman peaks partially varies for FX and MX, which holds especially true for the Raman peak located around 200 cm^{-1}. Nevertheless, the peak positions align well with the published literature and connect with the available -O, -(OH), and -F surface terminations on FX and MX nano-sheets. For both nano-sheets, the peaks at 125 and 129 cm^{-1} connect with the resonant mode (plasmonic peak), while in- and out-of-plane vibrations of titanium (E$_g$ and A$_{1g}$) connect with the subsequent peaks around 210 cm^{-1}. The rather broad Raman peaks between 230 and 470 cm^{-1} match with the E$_g$ modes of Ti$_3$C$_2$F$_2$, Ti$_3$C$_2$O$_{2,}$ and Ti$_3$C$_2$(OH)$_2$. The last peaks shown in the spectra can be assigned to E$_g$ and A$_{1 g}$ carbon modes.

3.2. Photothermal characterization and Biocompatibility of MX and FX

FX and MX (25, 50 and 100 μg/mL) were exposed to 808 nm laser irradiation for 3 min at three different power densities for both nano-sheets (2.3/1.3/0.6 W/cm^2 for MX and 1.3/0.8/0.4 W/cm^2 for FX at 25, 50 and 100 μg/mL, respectively) in buffer solution (Fig. 2 **a** and **b**). MX reached a temperature of 45 °C within 3 min at higher power densities than FX using the same concentration (Fig. 2 **a**), which implies a higher thermal conversion for FX. For PTT, the laser power was chosen to achieve the same temperature after 3 min of exposure for each
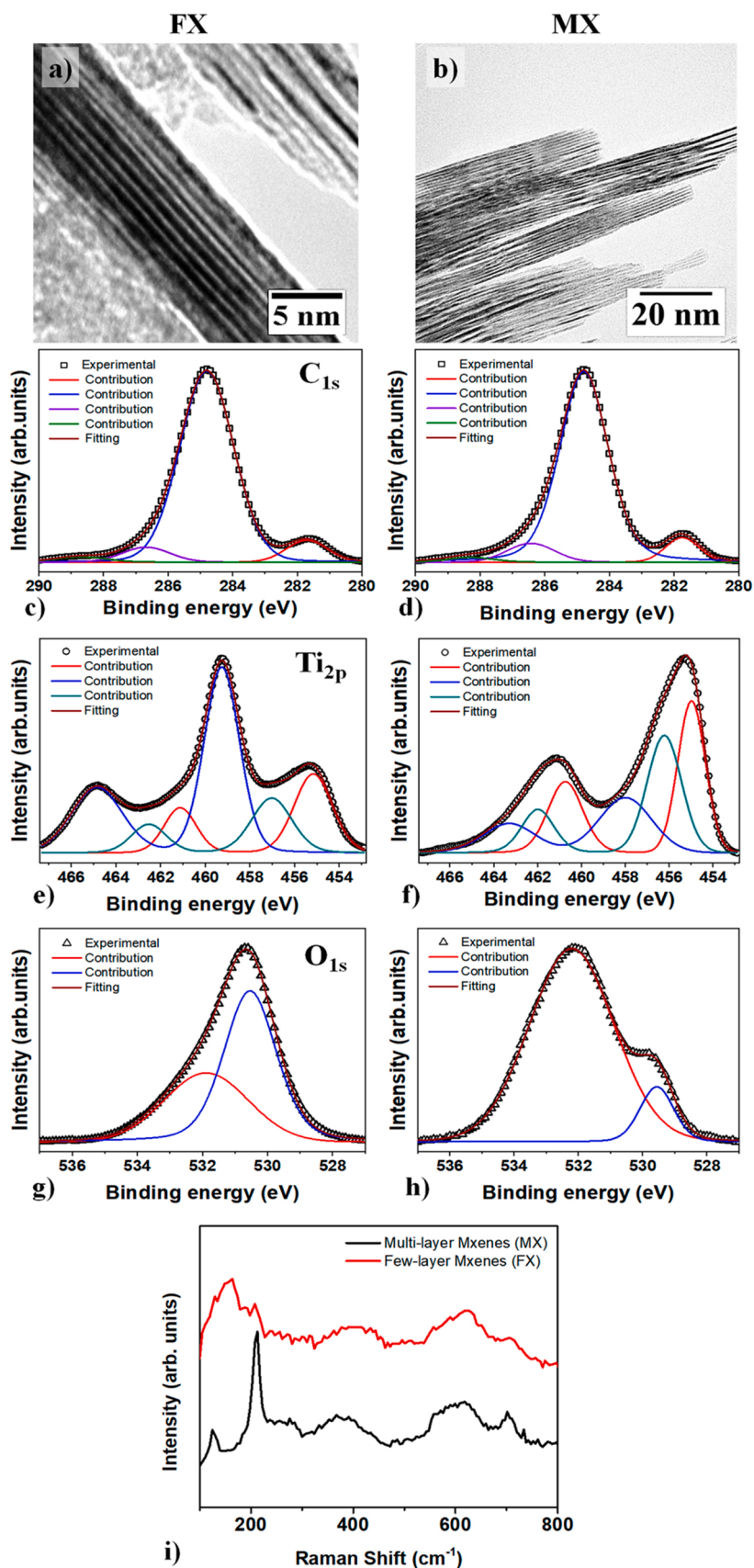
Fig. 1. Transmission electron micrographs of **(a)** few- and **(b)** multi-layer $Ti_3C_2T_x$ nanosheets. **(c)** Demonstrates the corresponding Raman spectra. Detailed XPS scans of the (c and d) C_{1s}, (e and f) Ti_{2p} and (g and h) O_{1s} region for (c, e, and g) few- and (d, f, and h) multi-layer $Ti_3C_2T_x$ nanosheets, respectively. For all XPS data, triangles represent the experimental raw data, while the peak fitting of different contributions is illustrated in different colors. The sum of all mathematical fits is displayed in the solid lines (fitting), which appropriately match the experimental data. **(i)** Comparison of the obtained Raman spectra for few- and multi-layer $Ti_3C_2T_x$ nanosheets.
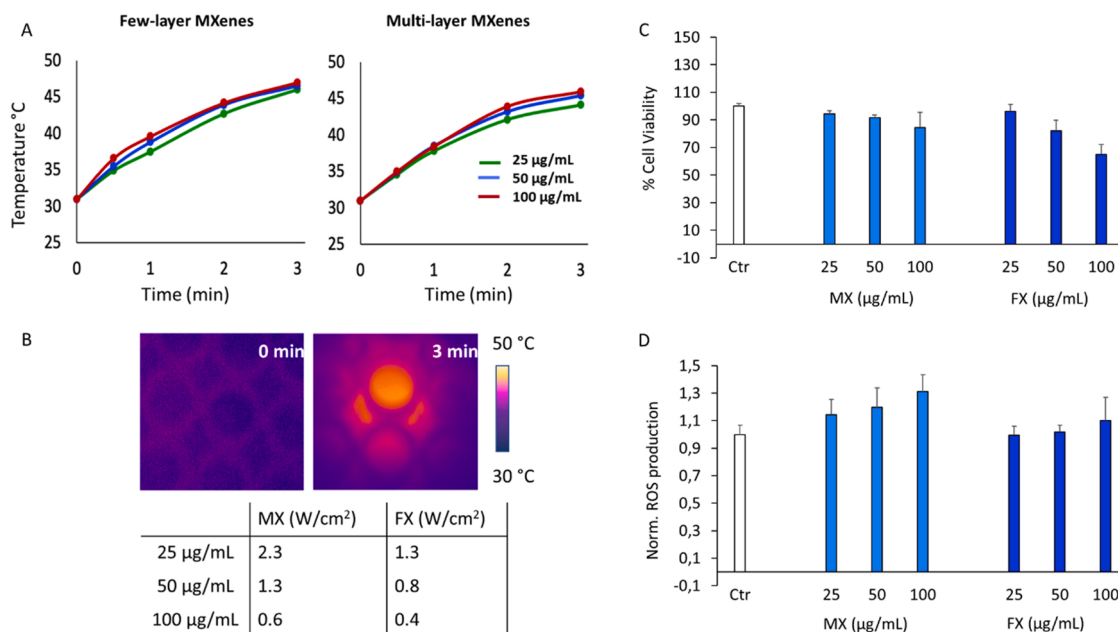
Fig. 2. The photothermal effect and biocompatibility of FX and MX on 2D model of 4T1. **(a)** Temperature increase measured on FX and MX after exposure to NIR laser for 3 min in buffer solution. Three concentrations of MXenes (25, 50 or 100 μg/mL) and different laser powers for each concentration (2.3/1.3/0.6 W/cm^2 for MX and 1.3/0.8/0.4 W/cm^2 for FX at 25, 50 and 100 μg/mL, respectively) were tested. **(b)** Representative image of the temperature increase measured using an infrared camera; **(c)** Cell viability of 4T1 after treatment with different concentrations of FX and MX, expressed as % towards control cells. **(d)** ROS production after treatment with different concentrations of FX and MX normalized by the number of viable cells.

concentration based upon our previous study [38].

To define the MXene concentration for the 3D models, we first assessed the range of biocompatibility of MXenes on a 2D cultures after an acute treatment (24 h). In this way, we defined the non-toxic concentration of FX and MX. We investigated the cytotoxicity of FX and MX to determine whether the number of layers affects the cell viability. Biocompatibility was evaluated in terms of cell viability and ROS production. The cytotoxicity was assessed after 24 h of treatment with 25, 50, and 100 μg/mL of FX or MX. Results are reported in Fig. 2 (c) as % of control (untreated) cells. Both nanomaterials demonstrated good biocompatibility on the 4T1 cell line. Interestingly, FX induced a higher cytotoxicity than MX, which holds especially true for a concentration of 100 μg/mL. For this concentration, MX reduced the viability up to 84.3 ± 11.1 %, while FX demonstrated a reduced viability of 65.3 ± 7.2 %.

We further investigated the formation of ROS to confirm cell viability. For this purpose, we employed H$_2$DCFDA test after 24 h of treatment for all concentrations tested. The results are reported in Fig. 2 **(d)**, while the data were normalized to the number of viable cells and compared to ROS produced by control (untreated) cells. At 100 μg/mL, MX increased the ROS production (1.31 ± 0.12), while FX at the same concentration induced a ROS production of 1.10 ± 0.16.

Summarizing, our data confirm that 2D nanomaterials have a good biocompatibility at concentrations below 50 μg/mL, which we defined as concentration for the subsequent experiments.

3.3. Photothermal therapy on 4T1 3D models

Subsequently, we investigated the effects of PTT on a more complex 3D culture model of breast cancer. This aspect is essential since 3D models accommodate many relevant biological characteristics, including different patterns of spheroid core growth and cell invasion into the surrounding ECM, when compared to standard 2D cultures. For this purpose, we produced two different 4T1 3D models such as conventional and bio-printed spheroids. The morphology and growth of bio-printed spheroids are consistently different from conventional spheroids. Therefore, it is crucial to evaluate both models by monitoring the

respective growth. The growth of conventional spheroids was evaluated regarding the increase of the radius, while the growth of the bio-printed spheroids was studied in terms of the increase of the radius and the spheroids' density (Fig. 3). The density was not evaluated for conventional spheroids since it remains constant over time. Results are reported in Fig. 3. The radius of the conventional spheroids increased over time up to 146.3 ± 2.38 % with respect to day 0. While the radius of the bio-printed spheroids embedded in the alginate matrix did not change over time, the cell density significantly increased after 20 days from bio-printing. This indicates that cells could proliferate and fill-in the ECM space. Consequently, we defined the start of PTT for bio-printed spheroids after 20 days of bioprinting.

After this detailed growth analysis, we administered MX or FX at 50 μg/mL following the experimental trends observed for the 2D models. The conventional and bio-printed spheroids were incubated with MXenes for 24 h before any further treatment. After incubation, we performed 3 min PTT at a power density of 0.47 and 0.3 W/cm^2 for cells treated with MX and FX, respectively, to reach the same temperature for all samples. We evaluated the effect of PTT using cell viability and ROS production. The viability and ROS production were characterized after 48 and 96 h from the administration of FX and MX at 50 μg/mL, which converts into 24 and 72 h after PTT considering the 24 h of incubation. Fig. 4 **(a)** reports the viability of conventional spheroids after MXenes-mediated PTT. The results are reported as % of control (untreated) cells. After an incubation time of 48 h, a significant reduction in the cell viability was observed for both spheroids (conventional and bio-printed) incubated with MX and FX when cells were irradiated with NIR light (Fig. 4**a** and **b**).

After 96 h, the reduction of viability was not enhanced compared to 48 h. In Fig. 4 **(b)**, the bio-printed spheroids' viability after PTT indicates a significant reduction in cell viability for both MX and FX. After 96 h from the administration of MXenes, an even stronger reduction in viability was observed in bio-printed spheroids treated with PTT. Indeed, bio-printed spheroids treated with MX and irradiated significantly reduced the viability up to 44.7 ± 5.80 %, while spheroids treated with FX and irradiated even further reduced the viability up to
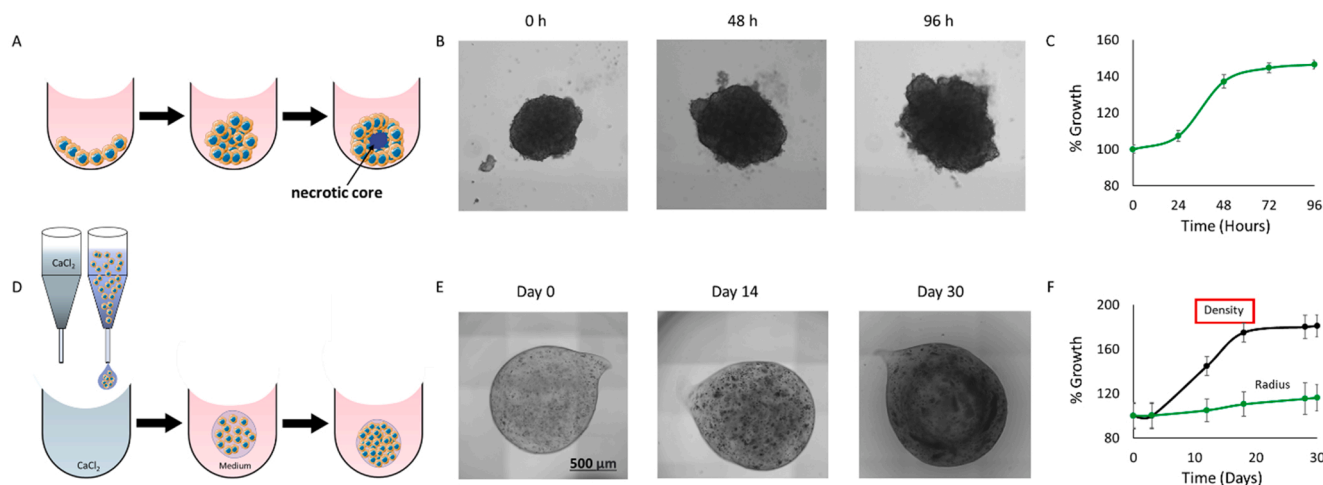
Fig. 3. Growth over time of 4T1 spheroids. **(a)** Representative illustration of the production process of conventional spheroids in a 96 well ULA plate. **(b)** Growth of conventional spheroids after centrifugation at 0, 48, and 96 h. Cells were seeded on ULA plates and centrifuged at 300 g for 3 min. **(c)** Growth of conventional spheroids in terms of radius increment over time. **(d)** Bioprinting of spheroids **(e)** Representative images of bio-printed 4T1 spheroids after 0, 14 and 30 days. **(f)** Growth of bio-printed spheroids in terms of radius and density over time.
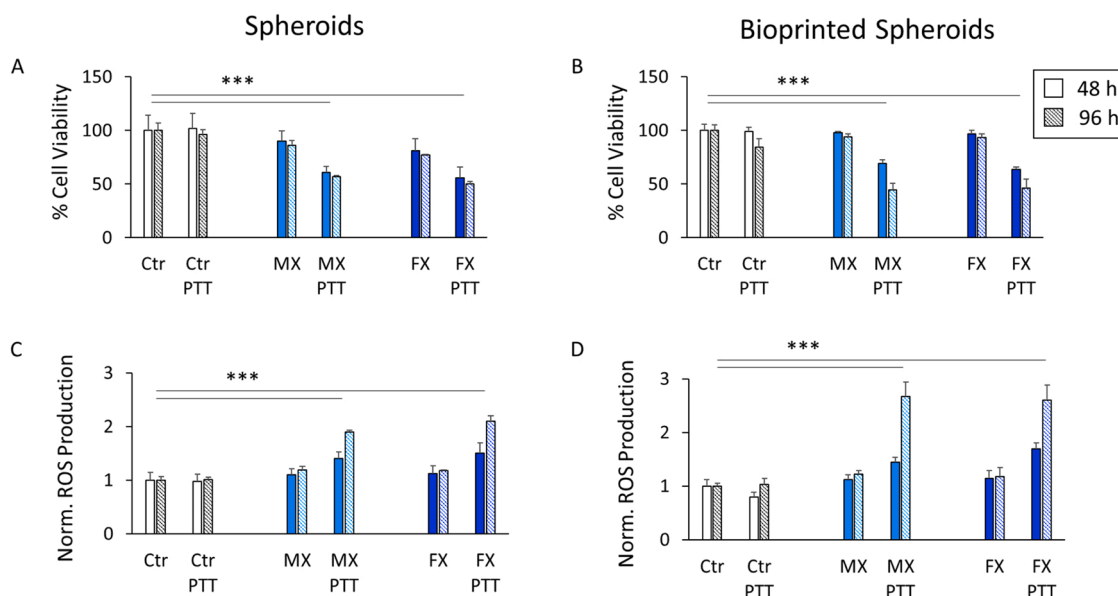

Fig. 4. Effect of PTT on both 4T1 spheroids and bio-printed spheroids. Viability of **(a)** conventional spheroids and **(b)** bio-printed spheroids after PTT at 48 and 96 h from the administration of MXenes, expressed as % of control cells. Production of ROS after PTT on **(c)** conventional and **(d)** bio-printed spheroids at 48 and 96 h from the administration of MXenes.

43.1 ± 8.45 %.

NIR radiation is known to cause an increase in the production of intracellular ROS, which occurs after stress caused by the rapid temperature increase [39]. Results of ROS production after 48 and 96 h from the administration of MXenes are reported for conventional and bio-printed spheroids in Fig. 4 **(c)** and **(d)**. Data were normalized by the number of viable cells and compared to ROS produced by control (untreated) cells.

After an incubation time of 48 h, the data in Fig. 4 **(c)** show that conventional spheroids treated with MX or FX maintained ROS levels comparable to control spheroids. When irradiated, spheroids treated with MX or FX increased ROS production up to 1.40 ± 0.12 and 1.50 ± 0.19, respectively. After 96 h and PTT, spheroids treated with MX and FX showed a notable increase in ROS production of 1.90 ± 0.02 and 2.10 ± 0.09, respectively.

The data presented in Fig. 4 **(d)** show that after 96 h and PTT

treatment, bio-printed spheroids strongly increased ROS production around 2.6 times compared to control cells.

3.4. Migration of RAW 264.7 and EA.hy926 by PTT

Other key aspects observed for most cancer regions are the systemic downregulation of immunological response as well as the new growth in the vascular network, or neoangiogenesis, which is crucial for the proliferation and metastatic spread of cancer cells. Therefore, the aim of PTT in our work is to induce specific cell death on 4T1 to activate the immune system to recognize tumor cells. This may directly target the cancer region, thus minimizing the non-specific inflammatory response that can seriously affect the breast architecture and physiology.

To observe the immune response, we treated 4T1 spheroids and 4T1 bio-printed spheroids with PTT and MXenes before collecting the supernatant after 96 h. The supernatant was transferred to a transwell

system containing RAW 264.7 cells to investigate changes in their migration. The results of macrophage migration on conventional 4T1 and bio-printed spheroids are shown in Fig. 5 **(a) and (b)**. The data are normalized by macrophages that migrated towards the supernatant of control (untreated spheroids).

Fig. 5 **(a)** shows the migration rate of macrophages towards the supernatant of conventional spheroids treated with FX and MX resulting a similar rate compared to the control cells (1.2 ± 0.02 and 1.16 ± 0.01 respectively). However, after PTT, the supernatant treated with MX and FX had a significant increase of the migration rate of macrophages (2.25 ± 0.26 and 1.62 ± 0.07, respectively), which implies a strong immune response due to the release of tumor-associated antigens. Fig. 5 **(b)** shows the migration of macrophages cells for bio-printed 4T1 spheroids after the treatment with MXenes-mediated PTT. The migration rate of the macrophages towards the supernatant of the bio-printed spheroids treated with MX and FX was similar compared to the control cells (1.3 ± 0.2 and 1.12 ± 0.02 respectively). Again, after PTT, a significant increase of the migration of macrophages was observed (2.15 ± 0.04 and 1.60 ± 0.1, respectively), which confirmed the data obtained for the conventional spheroids and underlines the reactivation of immune response.

Finally, to evaluate the potential induction of neoangiogenesis, the migration of endothelial cells after treatment of 4T1 and 4T1 bio-printed spheroids with PTT was evaluated. The respective results are demonstrated in Fig. 5 **(c) and (d)** and the data were normalized by endothelial cells that migrated towards the supernatant of control (untreated) tumor 3d models. Fig. 5 **(c)** shows the migration rate of endothelial cells towards the supernatant of conventional spheroids treated with MX and FX, which resulted in similar rates than the control cells (0.89 ± 0.15 and 0.98 ± 0.12, respectively). After PTT, the supernatant of 4T1 spheroids treated with MX and FX demonstrated a significant inhibition of the migration of endothelial cells. The migration rate of endothelial cells towards the supernatant of spheroids treated with MX and FX was reduced to 0.51 ± 0.03. and 0.57 ± 0.05, respectively. This indicates a possible inhibition of neo-angiogenesis mediated by PTT on spheroids treated with MXenes that needs further exploration in following-up studies. Fig. 5 **(d)** depicts the migration rate of endothelial cells towards the supernatant of bio-printed spheroids treated with MX and FX compared with the behavior of control cells (0.9 ± 0.05 and 0.86 ± 0.07, respectively). After PTT, the supernatant of 4T1 bio-printed spheroids treated with MX and FX showed again a significant inhibition of the migration of endothelial cells with reduced rates of 0.55 ± 0.08 and 0.49 ± 0.01, respectively. Recent studies have revealed that PTT is involved in several physiological and pathological interactions, including angiogenesis. PTT is known to decrease one of the main molecular markers of angiogenesis, VEGF-A [40]. Moreover, cell invasion assays and histological analysis demonstrated a reduction in migration of endothelial cells as well as the formation of novel blood vessels both *in-vitro* and *ex-vivo* after PTT [41,42]. The results of these studies align well with our findings.

Our data demonstrate the potential of MXenes as photosensitizing agents, capable of exerting a strong photothermal effect specifically on cancer cells in a 3D model capable of resembling tumor physiology along with its interactions with surrounding ECM components. Furthermore, we demonstrated that stimuli from spheroids embedded in physiological ECM after PTT had a strong effect on macrophage homing and inhibition of endothelial cells' migration towards the cancer region.

4. Conclusions

MXenes are emerging 2D nanomaterials recently exploited as photothermal agents for tumor ablation by PTT. Therefore, this study aimed at evaluating MXene-mediated PTT on two types of 3D models that resemble *in-vivo* structural complexity such as standard and bio-printed spheroids. Based on our experiments, we observe a strong reduction in cell viability and ROS production after irradiation, thus demonstrating MXenes' strong efficiency in non-invasive PTT on conventional 3D model spheroids. Interestingly, an even higher effect has been observed when MXene-mediated PTT was tested on the bio-printed spheroids, probably due to the presence of the ECM that can increase the thermal
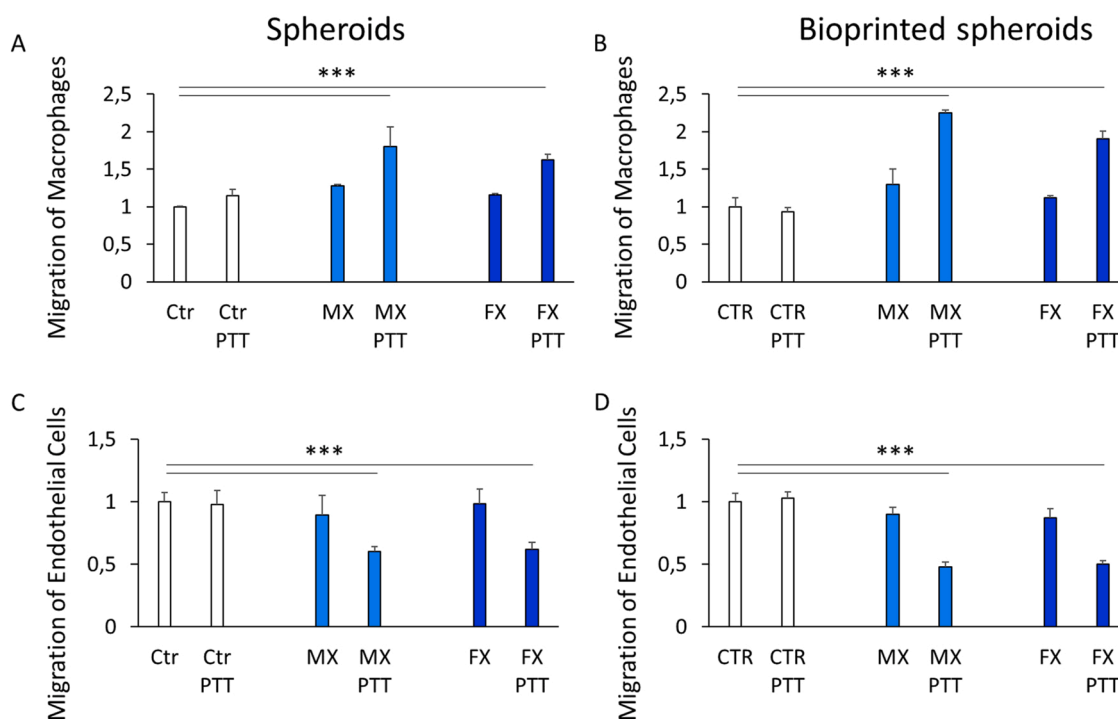

Fig. 5. Migration rate of macrophages or endothelial cells towards the supernatant of both 3D models treated with MX and FX. RAW 264.7 macrophages migration towards the supernatant of **(a)** conventional and **(b)** bio-printed spheroids after PTT. Number of endothelial cells' migrating towards the supernatant of **(c)** conventional and **(d)** bio-printed spheroids after PTT.

conduction and resemble more adequately the efficacy of PTT *in-vivo*. Moreover, the effect of the photothermal conversion was also investigated in terms of migration of the immune and endothelial cells towards cancer cells. Our experiments verify a significant increase in macrophages' migration towards the supernatant of irradiated bio-printed spheroids as well as an inhibition on endothelial cells. Considering all these aspects together underlines the potential of MXenes as photosensitizing agents, capable of exerting a strong photothermal effect and macrophage homing. We anticipate that this will further stimulate and boost future studies on potential immunotherapeutic strategies based on MXenes-mediated PTT, through a specific stimulation of the immune system against breast cancer with limited side effects. Furthermore, the inhibited migration of endothelial cells towards the irradiated cancer model paves the way for novel therapeutic strategies focused on the reduction of tumor neoangiogenesis.

CRediT authorship contribution statement

GP, AR, MP, Conceptualization. **GP, AR, GF**, Data curation. **GP, ER, DZ**, Formal analysis, Investigation. **GP, AR, DZ, AA**, Methodology. **AR, MP, MDS**, Project administration, Resources, Supervision. **GP, GF, MP, VP, AR**, Visualization, Writing – original draft. **GP, GF, MP, VP, AR**, Writing – review & editing.

Data Availability

Data will be made available on request.

Acknowledgements

References

[1] L.A. Torre, F. Islami, R.L. Siegel, E.M. Ward, A. Jemal, Global cancer in women: burden and trends, Cancer Epidemiol. Prev. Biomark. 26 (2017) 444–457.

[2] L. Siegel Rebecca, Miller Kimberly, D. Jemal Ahmedin, Cancer statistics, 2019, CA Cancer J. Clin. 69 (2019) 7–34.

[3] A.I. Fraguas-Sánchez, I. Lozza, A.I. Torres-Suárez, Actively targeted nanomedicines in breast cancer: from pre-clinal investigation to clinic, Cancers 14 (2022) 1198.

[4] G. Perini, et al., Functionalized graphene quantum dots modulate malignancy of glioblastoma multiforme by downregulating neurospheres formation, C 7 (2021) 4.

[5] V. Palmieri, et al., Reduction and shaping of graphene-oxide by laser-printing for controlled bone tissue regeneration and bacterial killing, vol. 5, 2018, 15027.

[6] F. Bugli, et al., Curcumin-loaded graphene oxide flakes as an effective antibacterial system against methicillin-resistant Staphylococcus aureus, Interface Focus 8 (2018).

[7] G. Perini, V. Palmieri, G. Ciasca, M. De Spirito, M. Papi, Unravelling the potential of graphene quantum dots in biomedicine and neuroscience, Int. J. Mol. Sci. 21 (2020) 3712.

[8] G. Perini, et al., Enhanced chemotherapy for glioblastoma multiforme mediated by functionalized graphene quantum dots, Materials 13 (2020) 4139.

[9] D. Zhi, T. Yang, J. O'hagan, S. Zhang, R.F. Donnelly, Photothermal therapy, J. Control. Release (2020).

[10] H.S. Kim, D.Y. Lee, Near-infrared-responsive cancer photothermal and photodynamic therapy using gold nanoparticles, Polymers 10 (2018) 961.

[11] M.V. Padalkar, N. Pleshko, Wavelength-dependent penetration depth of near infrared radiation into cartilage, Analyst 140 (2015) 2093–2100.

[12] H. Lin, Y. Chen, J. Shi, Insights into 2D MXenes for versatile biomedical applications: current advances and challenges ahead, Adv. Sci. 5 (2018), 1800518.

[13] G. Liu, et al., Surface modified Ti3C2 MXene nanosheets for tumor targeting photothermal/photodynamic/chemo synergistic therapy, ACS Appl. Mater. Interfaces 9 (2017) 40077–40086.

[14] A. Gazzi, et al., Photodynamic therapy based on graphene and MXene in cancer theranostics, Front. Bioeng. Biotechnol. 7 (2019) 295.

[15] H. Lin, S. Gao, C. Dai, Y. Chen, J. Shi, A two-dimensional biodegradable niobium carbide (MXene) for photothermal tumor eradication in NIR-I and NIR-II biowindows, J. Am. Chem. Soc. 139 (2017) 16235–16247.

[16] R.K. Jain, T. Stylianopoulos, Delivering nanomedicine to solid tumors, Nat. Rev. Clin. Oncol. 7 (2010) 653–664.

[17] L.-H. Han, J.H. Lai, S. Yu, F. Yang, Dynamic tissue engineering scaffolds with stimuli-responsive macroporosity formation, Biomaterials 34 (2013) 4251–4258.

[18] S. Roberts, S. Peyman, V. Speirs, Current and emerging 3D models to study breast cancer, Breast Cancer Metastasis Drug Resist. (2019) 413–427.

[19] J.L. Albritton, J.S. Miller, 3D bioprinting: improving in vitro models of metastasis with heterogeneous tumor microenvironments, Dis. Model. Mech. 10 (2017) 3–14.

[20] C. Moriconi, et al., INSIDIA: a FIJI macro delivering high-throughput and high-content spheroid invasion analysis, Biotechnol. J. 12 (2017), 1700140.

[21] G. Perini, et al., INSIDIA 2.0 high-throughput analysis of 3D cancer models: multiparametric quantification of graphene quantum dots photothermal therapy for glioblastoma and pancreatic cancer, Int. J. Mol. Sci. 23 (2022) 3217.

[22] S. Nath, G.R. Devi, Three-dimensional culture systems in cancer research: focus on tumor spheroid model, Pharm. Ther. 163 (2016) 94–108.

[23] Y. Kang, P. Datta, S. Shanmughapriya, I.T. Ozbolat, 3D bioprinting of tumor models for cancer research, ACS Appl. Bio Mater. 3 (2020) 5552–5573.

[24] W. Peng, et al., 3D bioprinting for drug discovery and development in pharmaceutics, Acta Biomater. 57 (2017) 26–46.

[25] I.T. Ozbolat, 3D Bioprinting: Fundamentals, Principles and Applications, Academic Press, 2016.

[26] I.T. Ozbolat, Scaffold-based or Scaffold-free bioprinting: competing or complementing approaches? J. Nanotechnol. Eng. Med. 6 (2015).

[27] W. Peng, D. Unutmaz, I.T. Ozbolat, Bioprinting towards physiologically relevant tissue models for pharmaceutics, Trends Biotechnol. 34 (2016) 722–732.

[28] S.A. DuPré, D. Redelman, K.W. Hunter Jr., The mouse mammary carcinoma 4T1: characterization of the cellular landscape of primary tumours and metastatic tumour foci, Int. J. Exp. Pathol. 88 (2007) 351–360.

[29] N. Torras, M. García-Díaz, V. Fernández-Majada, E. Martínez, Mimicking epithelial tissues in three-dimensional cell culture models, Front. Bioeng. Biotechnol. 197 (2018).

[30] B.B. Aggarwal, D. Danda, S. Gupta, P. Gehlot, Models for prevention and treatment of cancer: problems vs promises, Biochem. Pharm. 78 (2009) 1083–1094.

[31] M. Allen, Louise Jones, J. Jekyll and Hyde: the role of the microenvironment on the progression of cancer, J. Pathol. 223 (2011) 163–177.

[32] A. Rosenkranz, et al., Laser-mediated antibacterial effects of few-and multi-layer Ti3C2Tx MXenes, Appl. Surf. Sci. 150795 (2021).

[33] R.M. Sutherland, J.A. McCredie, W.R. Inch, Growth of multicell spheroids in tissue culture as a model of nodular carcinomas, J. Natl. Cancer Inst. 46 (1971) 113–120.

[34] M. Hu, et al., Surface functional groups and interlayer water determine the electrochemical capacitance of Ti3C2Tx MXene, ACS Nano 12 (2018) 3578–3586.

[35] J. Halim, et al., X-ray photoelectron spectroscopy of select multi-layered transition metal carbides (MXenes), Appl. Surf. Sci. 362 (2016) 406–417.

[36] M.V. Kuznetsov, S.V. Borisov, O.P. Shepatkovskii, Y.G. Veksler, V.L. Kozhevnikov, Investigation of TiC-C coatings by X-ray photoelectron spectroscopy, J. Surf. Investig. X-ray Synchrotron Neutron Tech. 3 (2009) 331–337.

[37] A.A. Galuska, J.C. Uht, N. Marquez, Reactive and nonreactive ion mixing of Ti films on carbon substrates, J. Vac. Sci. Technol. A Vac. Surf. Films 6 (1988) 110–122.

[38] A. Rosenkranz, et al., Laser-mediated antibacterial effects of few- and multi-layer Ti3C2Tx MXenes, Appl. Surf. Sci. 567 (2021), 150795.

[39] X. Zhan, et al., An NIR-activated polymeric nanoplatform with ROS- and temperature-sensitivity for combined photothermal therapy and chemotherapy of pancreatic cancer, Biomater. Sci. 8 (2020) 5931–5940.

[40] B.H. Marghani, A. Fehaid, A.I. Ateya, M.A. Ezz, R.M. Saleh, Photothermal therapeutic potency of plasmonic silver nanoparticles for apoptosis and anti-angiogenesis in testosterone induced benign prostate hyperplasia in rats, Life Sci. 291 (2022), 120240.

[41] X. Yang, et al., Near-infrared light-activated IR780-loaded liposomes for anti-tumor angiogenesis and photothermal therapy, Nanomed. Nanotechnol. Biol. Med. 14 (2018) 2283–2294.

[42] R. Fan, et al., Tumor acidity and near-infrared light responsive dual drug delivery polydopamine-based nanoparticles for chemo-photothermal therapy, Adv. Funct. Mater. 31 (2021), 2009733.